

---

APPROACH TO THE QUANTUM SIMULATION OF A  
ONE-DIMENSIONAL, INTERACTING BOSE GAS  
WITH A TUNABLE COUPLING QUBIT

INDIVIDUAL CONTROL OF  
COUPLING AND DETUNING

---

**Jonas Butscher**

Supervisor: Dr. Christopher Eichler  
Professor: Prof. Andreas Wallraff

Bachelor Thesis  
Quantum Device Lab  
ETH Zürich  
May 27, 2014



## Abstract

The goal of this thesis is to control the frequency of a qubit independent of its coupling strength to a microwave resonator, using magnetic flux control. For this purpose we describe the tunable coupling qubit (TCQ) and derive models to characterize this system by spectroscopic measurements. Further, in order to control the coupling strength and the detuning individually, we develop a calibration procedure to fit a non linear model. This model allows us then to calculate the magnetic flux for given qubit frequency and coupling strength. The qubit we use was designed in our lab (similar as proposed in Ref. [Gambetta11] and realised in Ref. [Srinivasan11]). It consists of a superconducting circuit, coupled to an on-chip microwave resonator. We plan to use this TCQ in the quantum simulation of a one-dimensional, interacting Bose gas in the Lieb-Liniger model (proposed by Ref. [Barrett13]). For this simulation a quantum mechanical two-level system, coupled to a cavity, is needed.

# Contents

<b>1</b>	<b>Introduction</b>	<b>1</b>
1.1	Motivation . . . . .	1
1.2	Quantum Simulation of a One-dimensional, Strongly Interacting Bose Gas	2
<b>2</b>	<b>Tunable Coupling Transmon</b>	<b>4</b>
2.1	The Transmon Qubit . . . . .	4
2.2	Tunable Coupling . . . . .	5
2.3	Electric Circuit Model . . . . .	7
2.4	Transmission mode . . . . .	8
2.4.1	Simplified Hamiltonian: Jaynes-Cummings Model . . . . .	8
2.4.2	Input-Output-Theory Approach . . . . .	9
<b>3</b>	<b>Measurement Setup</b>	<b>11</b>
3.1	Cryogenics . . . . .	11
3.2	Microwave Equipment . . . . .	11
3.2.1	Amplification . . . . .	12
3.2.2	Down-conversion . . . . .	12
3.3	Data Acquisition (ADC, FPGA) . . . . .	12
3.4	Coil and Flux-line . . . . .	13
<b>4</b>	<b>Individual Control of <math>\Delta</math> and <math>g</math></b>	<b>15</b>
4.1	Transmission Fit . . . . .	15
4.1.1	Peak Finding . . . . .	15
4.1.2	Initial Values . . . . .	16
4.1.3	Transmission Fit . . . . .	18
4.2	Linear Fit: B-Field Matrix . . . . .	18
4.2.1	Linear Model . . . . .	18
4.2.2	Fitting Routine . . . . .	18
4.2.3	Calibration Routine and Results . . . . .	20
4.3	Non Linear Model . . . . .	20
4.3.1	Taylor Expansion: New Fit Model . . . . .	21
4.3.2	Calibration Routine and Results . . . . .	21
4.4	Correlation Function Measurements . . . . .	22
4.4.1	First-Order Correlation Function $G^{(1)}$ . . . . .	22

4.4.2	Second-Order Correlation Function $G^{(2)}$ . . . . .	23
4.4.3	Measurements and Results . . . . .	23
<b>5</b>	<b>Outlook</b>	<b>25</b>
<b>A</b>	<b>Measurement Software</b>	<b>30</b>
A.1	SweepCleansweep . . . . .	30



# Chapter 1

## Introduction

### 1.1 Motivation

Despite the fast developments in high control of diverse quantum systems in quantum optics, as well as in solid state quantum physics in the last decades, the ultimate goal, the quantum computer still lies distant in the future. Nevertheless, these quantum systems do not only serve to study their fundamental quantum behaviour, but can also be used for quantum simulations.

Since simulating quantum systems with classical computers is computational time-intensive and for growing quantum system size the computational effort increases exponentially [Georgescu13], Feynman stated already more than 30 years ago

*"Let the computer itself be built of quantum mechanical elements which obey quantum mechanical laws."* [Feynman82, p. 474]

Although we have not yet developed an universal quantum simulator, it is already possible to simulate quantum physics with certain controllable quantum systems. Here, we prepare a quantum system, in form of a superconducting circuit, for the simulation of a quantum field with a continuous degree of freedom [Barrett13], unlikely to most other quantum simulations.

Proposed in Ref. [Barrett13] a cavity with a non linear medium inside with sufficiently strong interaction can simulate a gas of strongly interacting bosons. This is done by mapping the output field of the cavity on the spatial field operator of a one dimensional Bose gas. With this map, the mean energy of the Bose gas with respect to a variational state can be calculated. By minimizing this energy expression, the ground state can be found. Then in principle it is possible to measure all properties of the one dimensional, interacting Bose gas in its ground state by performing appropriate measurements on the cavity output field.

In our lab we work with superconducting qubits which are coupled to coplanar waveguide resonators. For Transmon qubits typically, the detuning of the qubit frequency and the resonator can be controlled by applying an external magnetic flux. However, the coupling strength depends on the geometrical design and therefore can not be changed, what is

essential for this kind of quantum simulation. Hence, we use a so called ‘‘Tunable Coupling Qubit’’ proposed by Ref. [Gambetta11]. This special qubit, which consists of two coupled Transmon qubits sharing a charge island, forms a hybridized state with tunable coupling, which we use together with the ground state as effective two-level system. This allows us to tune the coupling strength *and* the detuning of qubit and resonator individually.

The goal of this thesis is the implementation of the individual control of the coupling strength and the detuning of the tunable coupling qubit with respect to the resonator. This guarantees two degrees of freedom, which can be used to adjust our quantum system to operate it to the ground state of the mapped Hamiltonian, which we would like to simulate. Since the energy eigenstates of the one-dimensional interacting Bose gas with delta-interaction potential can be calculated analytically (Lieb-Liniger-Model), the Bose gas is ideal to test the reliability and accuracy of the quantum simulation. Further, the Bose gas can be simulated with classical computers and some attempts to experimentally realize it are made [Paredes04], such that a critical discussion of future results will be possible. This experiment can also be considered as a proof that controllable quantum systems can be used for more complicated simulations, which classical computers fail.

## 1.2 Quantum Simulation of a One-dimensional, Strongly Interacting Bose Gas

In 1963 Lieb and Liniger calculated the exact solutions of the stationary Schrödinger equation for an interacting Bose gas in one dimension [Lieb63] (the interaction was modelled as repulsive delta-function potentials). Hence, the ground state eigenfunction is known. This implies, that for delta-interaction potentials all properties of the ground state (e.g. the momentum distribution) can be calculated exactly, what enables a critical discussion of future results. Here, the concepts of this specific quantum simulation are reviewed.

Proposed by Ref. [Barrett13], a cavity with a driven, non linear medium inside can simulate the Hamiltonian of a one-dimensional, strongly interacting Bose gas in its ground state. Such a gas can be treated as quantum field with annihilation and creation operators,  $\psi(x)$  and  $\psi^\dagger(x)$ , obeying the canonical commutation relations  $[\psi(x), \psi^\dagger(y)] = \delta(x - y)$ . The Hamiltonian of this system has the form

$$H_B = \int (T + W + N) dx \quad (1.1)$$

where  $T = \frac{d\psi^\dagger(x)}{dx} \frac{d\psi(x)}{dx}$  describes the kinetic energy,  $W = \int w(x - y) \psi^\dagger(x) \psi^\dagger(y) \psi(x) \psi(y) dy$  the two-particle interaction with potential  $w(x - y)$  and  $N = -\mu \psi^\dagger(x) \psi(x)$  the chemical potential [Barrett13]. Now the crucial idea is to map the continuous output mode of the cavity onto the quantum state  $|\Psi(\lambda)\rangle$  of the one-dimensional field, where  $\lambda$  are variational parameters. This is done by linking the time dependency of the output field to the spatial dependency of the quantum field ( $t = x/s$ ). The scaling factor provides an additional variational parameter. Further, the annihilation operator  $\psi(x)$  is mapped on the field operator of the output field  $a_{\text{out}}(t)$ . The energy expression  $E(\lambda) = \langle \Psi(\lambda) | H | \Psi(\lambda) \rangle$



therefore translates to an expression in terms of the output mode. In case of the Lieb-Liniger model, the interaction potential is given by a delta function  $w(x - y) = v\delta(x - y)$ . Then the quantities, which have to be determined from the output mode, contain only first-order and second-order correlation functions. These correlations functions can be measured with the equipment in our lab [Lang11]. More precisely, the terms of  $E(\lambda)$  can be measured separately by

$$\langle T \rangle = \left\langle \frac{d\psi^\dagger(x)}{dx} \frac{d\psi(x)}{dx} \right\rangle \hat{=} \frac{1}{s^3} \int \omega^2 P_{a_{\text{out}}}(\omega) d\omega \quad (1.2)$$

$$\langle W \rangle = \langle \psi^\dagger(x)^2 \psi(x)^2 \rangle \hat{=} \frac{1}{s^2} G^{(2)}(0) \quad (1.3)$$

$$\langle N \rangle = \langle -\mu \psi^\dagger(x) \psi(x) \rangle \hat{=} -\frac{\mu}{s} G^{(1)}(0) \quad (1.4)$$

where  $G^{(1)}(\tau)$  and  $G^{(2)}(\tau)$  are the first and second order correlation function and  $P_{a_{\text{out}}}(\omega)$  is the power spectrum of the output field, which equals the Fourier transform of the first order correlation function ( $P_{a_{\text{out}}}(\omega) = \widehat{G^{(1)}}(\omega) = \int G^{(1)}(\tau) e^{-i\omega\tau} d\tau$ ). Once the energy expression is measured, it has to be minimized in dependence of the variational parameters  $\lambda$ . Here,  $\lambda$  consists of the coupling rate between cavity and non linear medium, drive power of the medium and the additional scaling factor  $s$ . This, for example, can be done with a standard numerical minimization method.

# Chapter 2

## Tunable Coupling Transmon

The qubits we use here are so called Transmon qubits. They can be used as effective two-level systems due to their anharmonicity. Typically, these qubits are coupled to a coplanar waveguide resonator. The transition frequency of the Transmon qubit can be adjusted by an external magnetic flux and hence can be tuned on- and off-resonant with the resonator. The interaction rate with the resonator depends on the geometric design of the circuit and is therefore fixed. When using the Transmons as a qubit, this is sufficient, since one usually wants to be in the strong coupling limit. However, for the purpose of the here aimed quantum simulation, it is necessary to tune the interaction strength  $g$  between qubit and resonator around the resonator decay rate  $\kappa$  to tune continuously from the strong coupling limit ( $g \gg \kappa$ ) into the bad cavity limit ( $g \ll \kappa$ ).

### 2.1 The Transmon Qubit

The Transmon qubit consists of two parallel Josephson junctions. These Josephson junctions consist of a small insulating gap between two superconductors. The Hamiltonian of a single Josephson junction has the form [Koch07]

$$H_J = 4E_C(n - n_g)^2 - E_J \cos(\phi), \quad (2.1)$$

where  $n$  is the number operator of tunneled Cooper pairs,  $n_g$  is the offset charge in units of  $2e$  and  $\phi$  is the superconducting phase drop across the tunnel barrier [Koch07]. The charging energy  $E_C = e^2/2C$  can be chosen very small compared with the Josephson energy  $E_J$ , since the total capacitance of the junction  $C$  can be increased by adding a large parallel capacity. This suppresses charge noise due to noise on  $n_g$  exponentially. Although for enlarging  $E_J/E_C$  the anharmonicity decreases with the square root of  $E_J/E_C$ . This ratio can be chosen appropriately, such that the charge noise is low and the anharmonicity is sufficiently large at the same time, since the noise suppression scales exponentially [Koch07].

By operating two parallel Josephson junctions in a so called SQUID loop, this circuit behaves as a single Josephson Junction with an effective Josephson energy of  $E_J = E_{J,\max} |\cos(\pi\Phi/\Phi_0)|$ , where  $\Phi$  is the external magnetic flux through the loop and

$\Phi_0 = h/2e$  is the magnetic flux quantum. This flux dependency allows to tune the Josephson energy and therefore the transition frequency between the two lowest energy eigenstates. These states are used as two-level system with transition frequency  $\omega_{ge} \approx \sqrt{8E_J E_C/\hbar} - E_C/\hbar$ , where  $g$  is the ground state and  $e$  the first excited state [Koch07].

## 2.2 Tunable Coupling

The tunable coupling Transmon (TCQ) is designed to have a tunable coupling strength to a microwave resonator and a tunable transition frequency [Gambetta11, Srinivasan11]. This is implemented with two coupled Transmon qubits with individual tunable frequencies ( $\omega_1$  and  $\omega_2$ ). The two Transmons share one charge island, while the other islands are capacitively coupled.

If both Transmons are tuned to the same frequency ( $\omega_1 = \omega_2$ ), the collective excitation states in the combined system can be seen as symmetric and antisymmetric modes in an oscillator picture (the oscillations can be pictured as charge, oscillating back and forth in the qubit). Hence, for the antisymmetric mode the interaction with the field in the resonator cancels out, since the charge distribution in qubit 1 and qubit 2 is opposite. This mode is called the dark state  $|d\rangle$  (with frequency  $\omega_-$ ), because it does not couple to the resonator. In contrast, the symmetric mode couples maximally to the resonator and is called bright state  $|b\rangle$  (with frequency  $\omega_+$ ). Now, if the relative detuning  $\delta$  of the two separate Transmons ( $\delta = \omega_1 - \omega_2$ ) is turned on, the dark and the bright state begin to mix. The dark state gets "brighter", i.e. the coupling is turned on and the bright state gets "darker" (weaker coupling), until the limit case, where both states have the same coupling. This allows us to tune the coupling of both states. The TCQ works with the ground and the dark state as an effective two-level system with variable coupling strength.

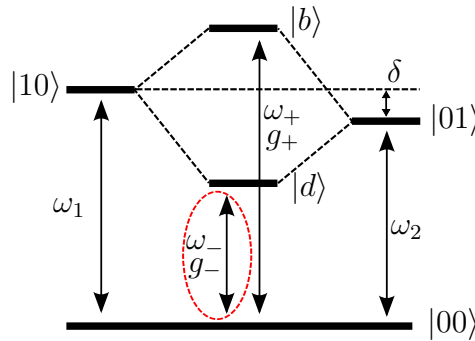


**Fig. 2.1:** Two coupled two-level systems with the hybridized states  $|b\rangle$  and  $|d\rangle$  (in our focus: dark state  $|d\rangle$  with frequency  $\omega_-$  and coupling strength  $g_-$  with respect to the resonator).

The design, which has been chosen here, is slightly different from the one used in Ref. [Srinivasan11]. Instead of two flux-lines, we have one flux-line located close to one of the

two SQUIDs (see Fig. 2.2) and a coil mounted on the sample holder, which couples to both SQUIDs equally. Furthermore, we have a charge line, which couples mainly to one of the Transmons (see Fig. 2.2). This charge line can be used to drive the qubit directly.

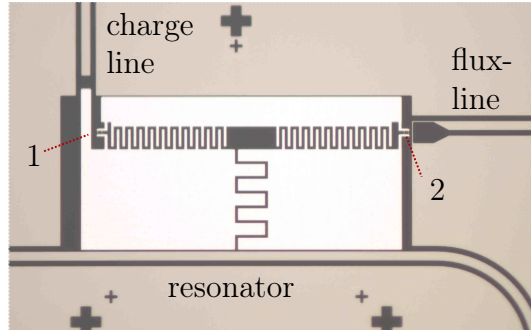


**Fig. 2.2:** TCQ design: all dark parts are insulating, whereas all light parts are superconducting (SQUID-loops: 1 and 2).

The total Hamiltonian of the system composed of the resonator, the TCQ and the interaction part is  $H = H_{\text{res}} + H_{\text{T}} + H_{\text{I}}$ . The TCQ Hamiltonian with the phases  $\phi_{1/2}$  across the two Josephson junctions yields in

$$H_{\text{T}} = \sum_{i=1,2} 4E_{C_i}(n_i - n_{g_i})^2 - \sum_{i=1,2} E_{J_i} \cos(\phi_i) + 4E_{\text{I}}n_1n_2 \quad (2.2)$$

where  $E_{\text{I}}$  is the interaction energy. The resonator and the qubit-resonator-interaction Hamiltonian have the form

$$H_{\text{res}} = \hbar\omega_r a^\dagger a \quad (2.3)$$

$$H_{\text{I}} = 2e^2 V_{\text{rms}}(\beta_1 n_1 + \beta_2 n_2)(-ia^\dagger + ia) \quad (2.4)$$

where  $\omega_r$  is the frequency of the resonator mode close to the qubit frequency,  $a^\dagger$  and  $a$  are the creation and annihilation operators of the resonator field,  $V_{\text{rms}}$  is the root mean square of the voltage fluctuations in the resonator [Srinivasan11] and  $\beta_i$  geometry dependent prefactors, which take in account that only a part of the voltage drop  $V_{\text{rms}}$  is over the Josephson junctions [Eichler13].

In the limit of  $E_{C_i}/E_{J_i} \ll 1$  the cosine in  $H_{\text{T}}$  can be expanded in good approximation, since the phases  $\phi_i$  are close to zero [Koch07]. The resulting TCQ Hamiltonian takes the form of two coupled anharmonic oscillators with frequencies  $\omega_{1/2}$ , anharmonicity  $\alpha_{1/2} \approx -E_{C_{1/2}}/\hbar$  and coupling constant  $J$  [Gambetta11].

For small  $\alpha_{1/2}/(\omega_+ - \omega_-)$  this Hamiltonian can approximately be diagonalized. With this transformation in the energy eigenbasis of the coupled system (dark and bright state), the effective Hamiltonian of the TCQ has the form

$$H_{\text{T}_{\text{eff}}} = \hbar \sum_{\pm} \left[ \omega_{\pm} + \frac{\alpha_{\pm}}{2} (b_{\pm}^\dagger b_{\pm} - 1) b_{\pm}^\dagger b_{\pm} \right] + \alpha_c b_+^\dagger b_+ b_-^\dagger b_-, \quad (2.5)$$

where  $b_{\pm}$  and  $b_{\pm}^{\dagger}$  are the annihilation and creation operators of the anharmonic oscillators in the eigenbasis approximation and  $\alpha_{\pm}$  are the corresponding anharmonicities. Note that the states corresponding to these annihilation and creation operators are the dark and the bright state mentioned above.  $\alpha_c$  is the strength of a cross Kerr effect between dark and bright state [Gambetta11].

Now we want to investigate the coupling of these modes to the resonator. With a rotating wave approximation on the anharmonic oscillator model we get the effective interaction Hamiltonian [Gambetta11]

$$H_{I_{eff}} = \sum_{\pm} g_{\pm}(ab_{\pm}^{\dagger} + a^{\dagger}b_{\pm}), \quad (2.6)$$

where  $g_{\pm} = g_{1/2} \cos(\lambda) \pm g_{2/1} \sin(\lambda)$ ,  $g_{1/2} = \sqrt{2}e^2\beta_{1/2}V_{rms}(E_{J_{12}}/8E_{C_{1/2}})^{1/4}$  and  $\lambda = \arctan(2J/\zeta)/2 + \theta$ , ( $\zeta = \omega_1 - \omega_2 - (\alpha_1 - \alpha_2)/2$ ,  $\theta = \pi/2$  for  $\zeta < 0$  and  $\theta = \pi$  for  $\zeta > 0$ ) [Gambetta11].<sup>1</sup>

Thus, the analytic expression of our coupling strength of interest  $g_{-}$  is a rather complicated expression, which is later expanded in a Taylor series.

## 2.3 Electric Circuit Model

In order to design the chip with the desired parameters, the system is translated into an equivalent circuit model. When the qubits are approximated with harmonic oscillators, the electric circuit looks like in Fig. 2.3, where  $C_i$  are the capacities,  $L_i$  the inductances and  $\phi_i$  the flux nodes. The Lagrange function is then calculated by  $\mathcal{L} = \sum_i C_i \Delta \ddot{\phi}_i^2 / 2 - \Delta \phi_i^2 / 2L_i$ , where the sum is taken over all capacities and inductances. Further, the Hamiltonian is calculated by the Legendre transformation of the Lagrangian. For this circuit and a given design, the capacitances can be calculated with a finite element software (MAXWELL). With the transformation described above, the coefficients of the Hamiltonian, such as the charging energies  $E_{C_j}$ , the Josephson energies  $E_{J_j}$  and the interaction energy  $E_I$  can be estimated. This is used to find a design with the desired system parameters.

---

<sup>1</sup> $\omega_{1/2} = \sqrt{8E_{J_{1/2}}E_{C_{1/2}}}/\hbar - E_{C_{1/2}}/\hbar$ ,  $\alpha_{1/2} = -E_{C_{1/2}}/\hbar$   
 $\omega_{\pm} = \omega_{1/2} + (\alpha_{\pm} - \alpha_{1/2})/2 + (\alpha_1 + \alpha_2)J^2/2\mu^2 \pm \mu/2 \mp \zeta/2$ ,  $\alpha_{\pm} = (\alpha_1 + \alpha_2)(1 + \zeta^2/\mu^2)/4 \pm \zeta(\alpha_1 - \alpha_2)/2\mu$ ,  
 $\mu = \sqrt{4J^2 + \zeta^2}$  [Gambetta11].

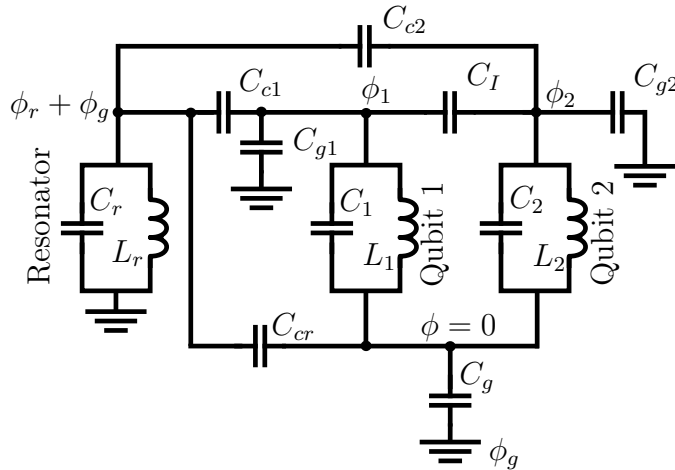


**Fig. 2.3:** Electric circuit equivalent of the TCQ: Resonator and qubits are represented by capacitively coupled LC resonators.

## 2.4 Transmission mode

Aiming to derive the frequency dependency of the transmission of the resonator, we will first simplify our system Hamiltonian as a harmonic oscillator in the weak drive limit (only lowest level occupied) coupled to a single mode of the resonator with frequency close to the qubit transition frequency ( $|00\rangle \rightarrow |d\rangle$ ). Then we will use input-output-theory to derive an analytical expression for the frequency depending transmission of the two sided resonator.

### 2.4.1 Simplified Hamiltonian: Jaynes-Cummings Model

In a first approximation one can only consider the ground state  $|00\rangle$  and the dark state  $|d\rangle$  of the TCQ interfering with the resonator. The simplified model Hamiltonian of the uncoupled qubit  $H_q$  (in harmonic approximation) and the resonator Hamiltonian  $H_{\text{res}}$ , respectively take the form (all higher orders and non linear terms neglected)

$$H_q \approx \hbar\omega_q b^\dagger b, \quad H_{\text{res}} = \sum_i \hbar\omega_{\text{res}}^i a_i^\dagger a_i, \quad (2.7)$$

where  $a_i^\dagger$  and  $a_i$  are the creation and the annihilation operators of the electromagnetic field in the resonator and  $b^\dagger$  and  $b$  are the raising and lowering operators of the qubit. For the interaction term, only the resonator mode with frequency close to the qubit frequency  $\omega_{\text{res}} \equiv \omega_{\text{res}}^i \approx \omega_q$  is considered. Then the interaction Hamiltonian assumes the form of the typical Jaynes-Cummings interaction

$$H_{\text{int}} = \hbar g(b^\dagger a + ba^\dagger), \quad (2.8)$$

where  $g$  is the coupling constant. The total Hamiltonian of the system is then given by

$$H_{\text{JC}} = \hbar\omega_{\text{q}}b^\dagger b + \hbar\omega_{\text{res}}a^\dagger a + \hbar g(b^\dagger a + ba^\dagger). \quad (2.9)$$

To give a rough estimate of the hybrid state eigenenergies for low drive power, one can neglect all higher resonator excitations and calculate the energies. The estimated eigenenergies (with renormalized energy  $E_{|00\rangle} = 0$ ) are then approximated by

$$\omega_{\pm} = \frac{(\omega_{\text{res}} + \omega_{\text{q}}) \pm \sqrt{\Delta^2 + 4g^2}}{2}, \quad (2.10)$$

where  $\Delta \equiv \omega_{\text{res}} - \omega_{\text{q}}$ .

### 2.4.2 Input-Output-Theory Approach

For the transmission line (analogous to a two sided cavity [Walls08]), the relation between output field and field in the resonator can be simplified to

$$\alpha_{\text{out}}(t) = \sqrt{\kappa}\alpha(t), \quad (2.11)$$

if the coupling to the output port is much larger than the coupling to the input port (further incoming fields through the output port are neglected).

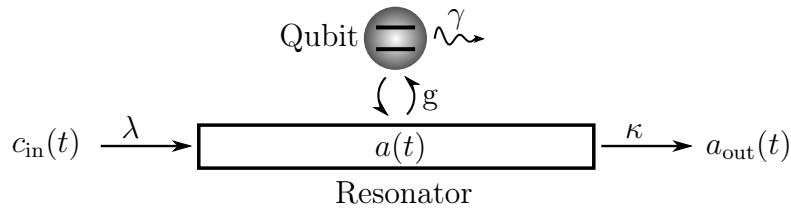


**Fig. 2.4:** Resonator with input field  $c_{\text{in}}(t)$  and output field  $a_{\text{out}}(t)$  which are capacitively coupled to the resonator mode  $a(t)$  with the rates  $\lambda$  and  $\kappa$ , respectively. The qubit with internal decay rate  $\gamma$  is capacitively coupled to the resonator with interaction strength  $g$ .

The equations of motion in the Schrödinger picture in the this approximation are

$$\dot{a}(t) = -\frac{i}{\hbar}[a(t), H_{\text{syst}}] - \frac{\kappa}{2}a(t) + \sqrt{\lambda}c_{\text{in}}(t) \quad (2.12)$$

$$\dot{b}(t) = -\frac{i}{\hbar}[b(t), H_{\text{syst}}] - \frac{\gamma}{2}b(t) \quad (2.13)$$

where  $\kappa$  is the decay rate of the resonator into the output port,  $\gamma$  the decay rate of the qubit state and  $\lambda$  the coupling strength of the input port ( $\lambda \ll \kappa$ ) [Walls08] (compare Fig. 2.4).

To solve these equations, it is useful to define the Fourier components

$$\begin{aligned} a(\omega) &= \frac{1}{\sqrt{2\pi}} \int_{\mathbb{R}} a(t) e^{i\omega t} dt, & b(\omega) &= \frac{1}{\sqrt{2\pi}} \int_{\mathbb{R}} b(t) e^{i\omega t} dt, \\ c_{\text{in}}(\omega) &= \frac{1}{\sqrt{2\pi}} \int_{\mathbb{R}} c_{\text{in}}(t) e^{i\omega t} dt, \end{aligned} \quad (2.14)$$

which results in

$$-i\omega a(\omega) = -i\omega_{\text{res}} a(\omega) - igb(\omega) - \frac{\kappa}{2} a(\omega) + \sqrt{\lambda} c_{\text{in}}(\omega), \quad (2.15)$$

$$-i\omega b(\omega) = -i\omega_{\text{q}} b(\omega) - iga(\omega) - \frac{\gamma}{2} b(\omega). \quad (2.16)$$

Solving those equations gives the transmission coefficient

$$S_{21}(\omega) \equiv \frac{a_{\text{out}}(\omega)}{c_{\text{in}}(\omega)} = \frac{\sqrt{\kappa}\sqrt{\lambda}}{i(\omega_{\text{res}} - \omega) + \frac{g^2}{i(\omega_{\text{q}} - \omega) + \frac{\gamma}{2}} + \frac{\kappa}{2}}, \quad (2.17)$$

of which we measure the absolute square  $T(\omega) \equiv |S_{21}(\omega)|^2$ . This function is plotted for realistic system parameters in Fig. 2.5.

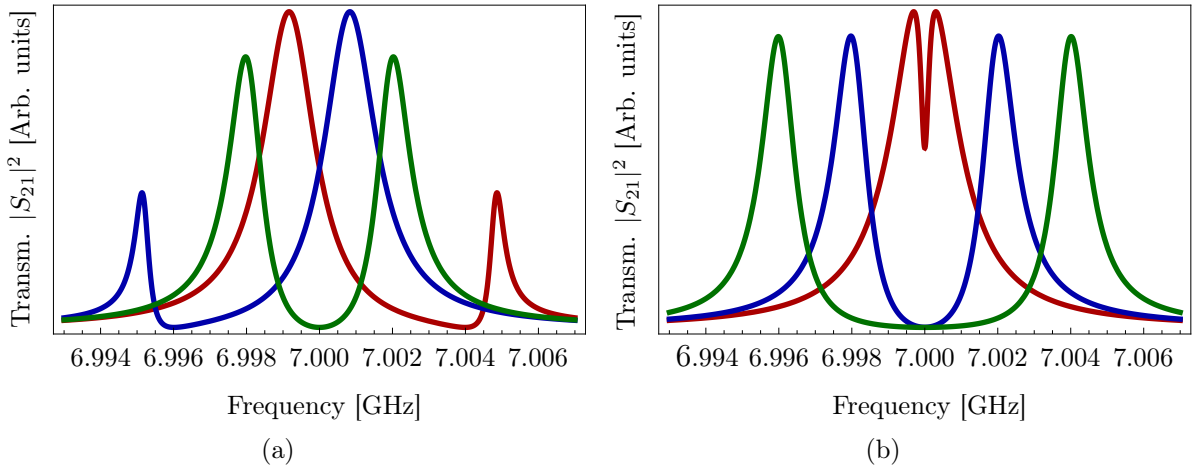


**Fig. 2.5:** Calculated transmission  $|S_{21}(\omega)|^2$  with  $\kappa/2\pi = 2$  MHz,  $\gamma/2\pi = 200$  kHz and  $\omega_{\text{res}}/2\pi = 7$  GHz for the coupling rate  $g/2\pi = 2$  MHz and detuning  $\Delta = -g, 0, g$  in (a) and  $\Delta/2\pi = 0$ ,  $g/2\pi = \{0.2, 2, 4\}$  MHz in (b).



# Chapter 3

## Measurement Setup

One of the major challenges in controlling quantum systems is the decoupling from environment effects. To avoid thermal excitations, we cool down our system. With state-of-the-art cryostats temperatures below 20 mK are achieved, such that we can go below  $E_{\text{thermal}}/E_{\text{q}} = \frac{k_{\text{B}}T}{\hbar\omega_{\text{q}}} < 0.06$ . I.e. the ratio of the probabilities for the qubit to be in the excited or in the ground state in thermal equilibrium,  $p_{\text{e}}/p_{\text{g}} = \exp(-\frac{\hbar\omega_{\text{q}}}{k_{\text{B}}T}) < 10^{-7}$ , is extremely low. That assures that the system will relax to the ground state in thermal equilibrium. Further, we will describe, how we control and read out our TCQ with microwave radiation and how the response of the quantum system is measured.

### 3.1 Cryogenics

To achieve such low temperatures, we use a cryostat which is structured in different levels with decreasing temperature for the lower levels (each level is separately thermally shielded, see Fig. 3.1). The system used here is a dry cryostat (OXFORD INSTRUMENTS Triton 200 cryostat), i.e. there is no bath of liquid helium inside. The cooling system consists of two different cooling stages. For the pre-cooling of the upper two levels (the 70 K and the 4 K plate), a pulse tube refrigerator is used. For lower temperatures, a  $^3\text{He}/^4\text{He}$  dilution refrigerator cools down the base plate (20 mK plate).

### 3.2 Microwave Equipment

To probe our system, we use microwave fields generated by commercially available microwave generators (AGILENT TECHNOLOGIES E8257C PSG Analog Signal Generator), which have controllable output frequency from 250 kHz up to 20 GHz with variable output power ( $-135$  dBm to 18 dBm). To measure the response of the chip, the signals have to be down-converted, since they are in the GHz range and hence too fast to be recorded by an analog-to-digital-converter (ADC). It is also important to have a amplification chain, which works as efficient as possible, such that data sets with adequate signal-to-noise ratio can be collected in an sensible amount of time.

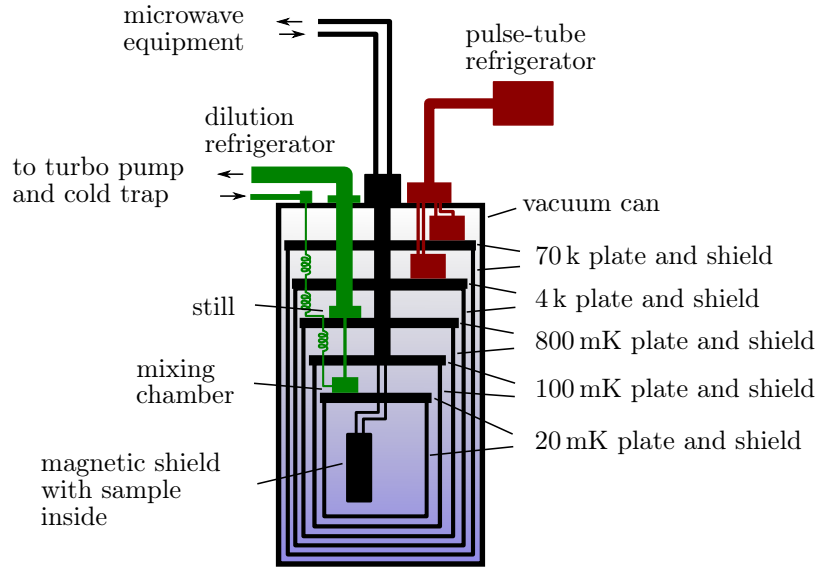


**Fig. 3.1:** Schematic of the cryostat (for detailed description see main text).

### 3.2.1 Amplification

When amplifying a weak signal, the noise added by the amplifier should be as small as possible. In our lab, we have on-chip amplifiers, called Josephson parametric dimer (JPD), whose noise level is near quantum limited [Eichler14]. They are placed next to the TCQ-chip in the bottom of the cryostat to reduce thermal noise (see Fig. 3.2). Then the signal is further amplified, first at the 4 K level with a cold HEMT (high-electron-mobility-transistor) amplifier and then at room temperature with low-noise amplifiers.

### 3.2.2 Down-conversion

To convert the fast oscillating output signal with frequency  $\omega_S$  (in the radio frequency (RF) range) down to frequencies measurable by the ADC, the signal is multiplied with a reference signal of a second microwave generator, using a mixer. This down-conversion reference signal generator is called the local oscillator (LO) and has a frequency  $\omega_{LO}$  about 25 MHz off the signal frequency (see Fig. 3.2). The resulting signal contains two frequency components at  $\omega_{\pm} = \omega_{LO} \pm \omega_S$ . The low frequency part  $\omega_-$  appears at 25 MHz, which can be sampled with a 100 MHz ADC, whereas the high frequency part is filtered out by a low-pass filter.

## 3.3 Data Acquisition (ADC, FPGA)

After the down-conversion process, the continuous, analogue signal is digitalized with a 14-bit analog-to-digital converter ADC (sampling rate  $f_{\text{samp}} = 100$  MHz). This resolution

of the ADC generates a data stream of more than 100 MB/s, which would accumulate a huge amount of data (some GB per measurement). To provide an useful form of the information, the data stream is processed in real time on a field-programmable gate array (FPGA). On the FPGA, the signal is multiplied with a 25 MHz sine and cosine, which results in a real and imaginary part of the signal, down-converted to 0 Hz. Further, this device allows us to perform different forms of data processing, such as averaging over many measurements and storing only the mean values, calculating continuously the auto-correlation and other applications (e.g.  $G^{(2)}$ -correlation measurements) [Lang11].

### 3.4 Coil and Flux-line

To control the external magnetic flux through the SQUID-loops, as mentioned in section 2.2, we use a coil mounted below the chip and an on-chip flux-line. These two devices are connected to separate DC-voltage sources (STANFORD RESEARCH SYSTEMS SIM928 batteries), which provide voltages in the range from  $-20$  V to  $20$  V by  $1$  mV steps. These batteries are connected to the coil and flux-line, respectively via low-pass filter and attenuator through a pair of twisted wires, to avoid induced currents by external stray fields. Further, the sample is shielded with a magnetic shield, since the TCQ is sensitive to magnetic fields.

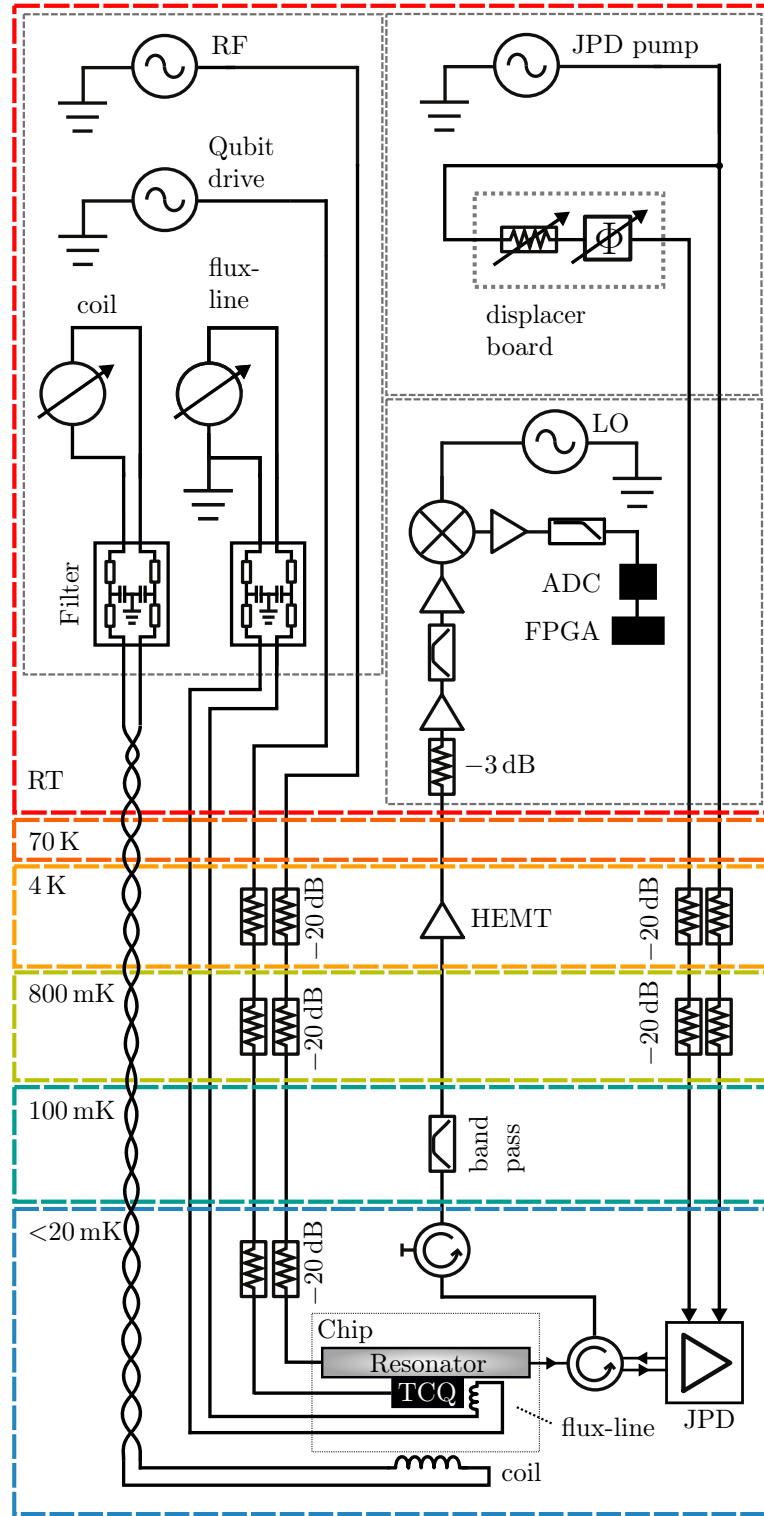


**Fig. 3.2:** Schematic of the measurement setup. For detailed description see main text.

# Chapter 4

## Individual Control of $\Delta$ and $g$

In order to control the coupling strength  $g$  and the detuning  $\Delta$  of our TCQ, we need a way to determine these values for a given B-field configuration. Then we need to generate a model, which links them to the two free parameters of our system (coil and flux-line voltage). The physical model, as derived in section 2.2 is a complicated formal relation. It would be necessary to fit many parameters, which is not desirable. Instead, we make a simplification around  $(\Delta, g) = (0, 0)$ , assuming linear behaviour. By fitting this linear relation, i.e. a two-by-two matrix, it is possible to invert the problem and determine the coil and flux-line voltage for given  $\Delta$  and  $g$ .

### 4.1 Transmission Fit

In section 2.4, the resonator transmission was derived as a function of the input frequency (see Eq. (2.11)). We use this model to fit our spectroscopic measurement data and extract the relevant system parameters ( $g, \omega_q, \omega_{\text{res}}, \kappa$  and  $\gamma$ ). For this spectroscopy, we send a radio frequency tone (RF) from the RF microwave generator to the resonator input and measure the averaged output field. Thereby, it is important to drive the resonator with low power to avoid qubit saturation. For a reliable fitting routine it is important to have adequate starting parameters. Hence, it is necessary to find the peaks in the data set, whose positions serve to calculate the start values for the fitting routine.

#### 4.1.1 Peak Finding

Even though for the human eye and brain it seems to be easy, a reliable way to find peaks in a given data set is a challenging task. In a first attempt, an existing peak-finding routine was used. This routine needs a threshold level as input and then searches for maxima above this threshold. If a maximum is found, the data points on both sides of this maximum down to the threshold level are cut out. This procedure is repeated until the specified number of peaks is found, or there are no more data points above the threshold level.

This routine works for a lot of data sets, but fails in some cases and therefore is not stable enough to be used. To improve the peak finding, the cases, where the routine described

above failed, were investigated. Two different causes for the peak finding failure were determined. First, there was the possibility, that peaks are misidentified due to noise (see Fig. 4.1(a)). Second, only one peak is found, although a second peak is clearly visible by bare eye, as illustrated in Fig. 4.1(b). There, the dip between the two peaks is very small and thus, the two peaks were identified as a single peak. For finding both peaks, the threshold level would have to be chosen in a way, such that the dip reaches below the threshold level. However, this is not useful, since this can be a different value for different data sets.

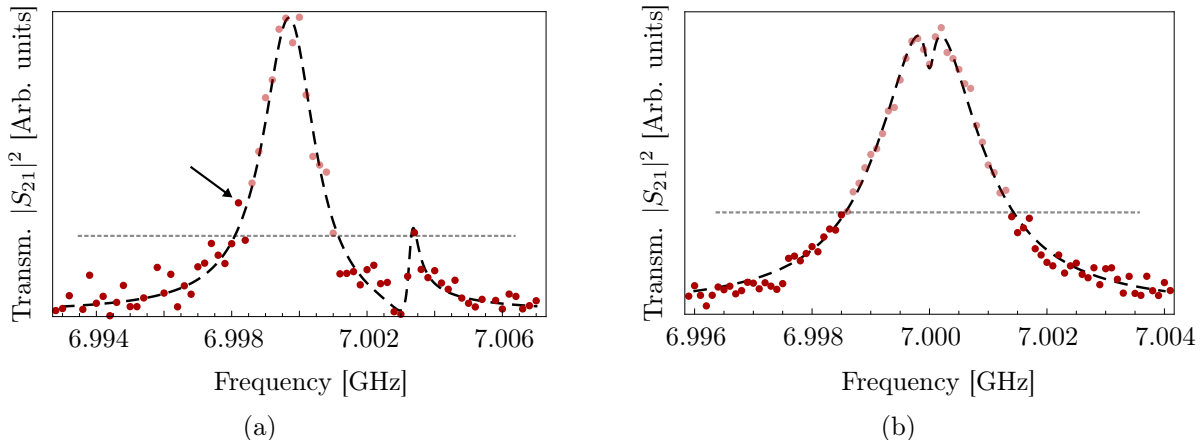


**Fig. 4.1:** Two possible ways for the peak-finding routine to fail (the grey dashed line is the threshold level). The transparent points are the ones, which are cut after the first peaks is found. In (a) a peak is misidentified due to noise (arrow), even tough the correct second peak is not below the threshold level. In (b) the close peaks could not be resolved, since the threshold level is too low.

As a solution for the first problem, a “noise suppression” input (integer number  $n$ ) was created, that cuts additional  $n$  data points away on both sides when a peak is found and the data points are deleted. In this way, such noise-peaks can be avoided. However, this noise suppression has to be handled carefully, since it could cut out important data points in case of very close peaks. For the second problem, where the peaks are very close, we came up with an iterative method to find the peaks. First, the threshold is set to a high level (e.g. 90% of the maximum of the data set). Then, the threshold is successively decreased until the peak-finding routine finds two peaks or a minimum threshold is reached. Although this process is more time consuming, it seems to pay off, since it finds the peaks reliably.

### 4.1.2 Initial Values

For a successful fit, it is essential to have reasonable start values. These are extracted from the peak positions, determined in the last section. With Eq. (2.10) we can approximate

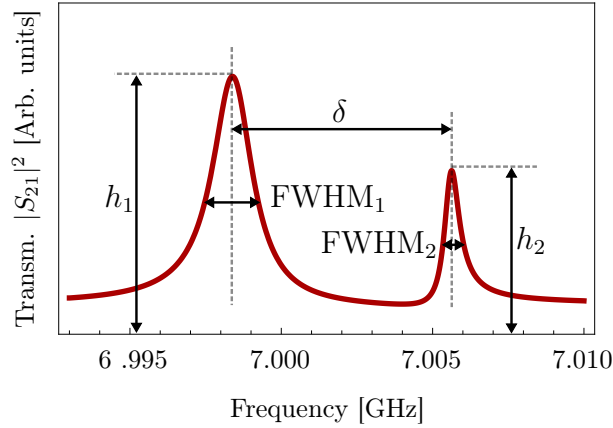


**Fig. 4.2:** Schematic of the transmission, where  $\delta$  indicates the distance between the peaks,  $h_i$  the peak heights and  $\text{FWHM}_i$  are the width of the peaks at half of the height.

the distance between the peaks  $\delta$  and the average peak frequency  $\bar{\omega}$  (compare Fig. 4.2).

$$\delta = \sqrt{(\omega_{\text{res}} - \omega_{\text{q}}) + 4g^2}, \quad \bar{\omega} = \frac{\omega_{\text{res}} + \omega_{\text{q}}}{2} \quad (4.1)$$

Moreover, the difference  $d$  of the square root of the peak heights  $h_1$  and  $h_2$  (see Fig. 4.2) is given up to first order in  $\gamma/\kappa$  and second order in  $\Delta$  by [Winterer13]

$$d = \sqrt{h_1} - \sqrt{h_2} = \frac{4\Delta}{J} \frac{\gamma}{\kappa}. \quad (4.2)$$

These equations can be inverted to calculate approximations for  $g$ ,  $\omega_{\text{res}}$  and  $\omega_{\text{q}}$ . Since  $d$  and  $\bar{\omega}$  can be estimated from the peak positions and  $\lambda$  is approximated by  $\lambda \approx \frac{1}{4} \text{Max}$  ( $\text{Max}$  is the maximum height of the two peaks), we can calculate estimations for  $g$ ,  $\omega_{\text{res}}$  and  $\omega_{\text{q}}$  which are used as start values

$$g_{\text{start}} = \frac{4\delta}{\sqrt{64 + \frac{\kappa^2 d^2}{\gamma^2}}} \quad \text{and} \quad \omega_{\text{res/q,start}} = \frac{1}{2} \left( m \pm \frac{d\delta}{\sqrt{64\gamma^2 + d^2\kappa^2}} \right). \quad (4.3)$$

Further,  $\kappa_{\text{start}}$  is required as input variable (it can easily be determined as the FWHM of the resonator for large qubit detuning). An initial value for  $\gamma$  is calculated from the sum of the two FWHMs, since  $\kappa + \gamma \approx \text{FWHM}_1 + \text{FWHM}_2$  (see Fig. 4.2), i.e.  $\gamma_{\text{start}} = \text{FWHM}_1 + \text{FWHM}_2 - \kappa_{\text{start}}$ .

If only one peak is found, we set  $\Delta_{\text{start}} = 0$  (i.e.  $\omega_{\text{res}} = \omega_{\text{q}} = \omega_{\text{peak}}$ ). To cover the case, where despite the improved peak finding routine only one peak is identified for very small coupling ( $g \ll \kappa$ ) (compare cases in Fig. 4.1(b)),  $g_{\text{start}}$  is not set to zero (in fact,  $g_{\text{start}} \equiv \gamma_{\text{start}} \ll \kappa$ ). Here, we risk some error if it really was only one peak, but in return the fit routine is able to succeed for even smaller  $g$ .

### 4.1.3 Transmission Fit

Finally, all these pieces are put together in one function `CMTFit` (in `MATHEMATICA`) which automatically fits a transmission data set. As inputs, the function requires besides the absolute squared transmission, the according frequency vector and  $\kappa_{\text{start}}$  some other variables, which define e.g. the output form and the automatic generation of a PDF file of the plot. Important inputs are the `noisesuppression` number as described above, and the choice whether close peaks are expected or not (`closepeaksexpected`, turns the successive peak finding on and off). The input parameter `thresholdfactor` sets the threshold level according to

$$\text{threshold level} = \frac{1}{2} \sum_{i=1,2} \text{Mean}[T_i] + \text{thresholdfactor} \times \text{StandardDeviation}[T_i], \quad (4.4)$$

where  $T_{1/2}$  are the first and the last 10th of the transmission data set, respectively. The initial values are determined according to the previous section and the fit is finally calculated with the `MATHEMATICA` function `FindFit`.

## 4.2 Linear Fit: B-Field Matrix

In a next step, since we are now capable of determining  $\Delta$  and  $g$  for a given set of coil and flux-line voltages, we need a model for the relation between these voltages and the detuning and coupling rate. Once this relation is found by fitting to test data, it can be inverted to calculate the voltages  $B_c$  and  $B_{\text{fl}}$  for given  $\Delta$  and  $g$  (the voltages are here named  $B$  as the external flux is proportional to the voltage).

### 4.2.1 Linear Model

The Transmon frequencies  $\omega_1$  and  $\omega_2$  depend on the external flux with  $\cos(\pi\Phi_i/\Phi_0)$ . If the flux is only tuned in a small region ( $\Delta\Phi_i \ll \Phi_0$ ), then  $\omega_1$  and  $\omega_2$  can be expanded in  $\Phi_i$  linearly, i.e. the flux dependency is approximately linear. Further, if  $g \ll g_{\text{Transmon}}$  ( $g_{\text{Transmon}}$  is the intrinsic coupling rate of the Transmons), the expression of  $g = g_-$  should also be well approximated by linear terms. Hence, assuming only linear behaviour leads to a model of the form

$$\begin{pmatrix} \Delta \\ g \end{pmatrix} = \mathbf{M}(\vec{B} - \vec{B}_0) = \begin{pmatrix} m_{11} & m_{12} \\ m_{21} & m_{22} \end{pmatrix} \begin{pmatrix} B_c - B_{c,0} \\ B_{\text{fl}} - B_{\text{fl},0} \end{pmatrix}. \quad (4.5)$$

If the matrix  $\mathbf{M}$  and the vector  $\vec{B}_0$  are calculated with a linear fit, for given  $\Delta$  and  $g$  the voltages can be predicted:  $\vec{B} = \mathbf{M}^{-1}(\Delta, g)^T + \vec{B}_0$ .

### 4.2.2 Fitting Routine

Our standard measurement software allows us to perform a sweep of  $B_c$  for fixed  $B_{\text{fl}}$  and vice versa. With the linear model in Eq. (4.5) it is possible to perform a fit with only two



sweeps. Since we deal with a linear model here, we can use a linear least squares fit:

$$\begin{pmatrix} \Delta_0 \\ \Delta_1 \\ \vdots \end{pmatrix} = \begin{pmatrix} B_{c,0} & B_{fl,0} & 1 \\ B_{c,1} & B_{fl,1} & 1 \\ \vdots & \vdots & \vdots \end{pmatrix} \begin{pmatrix} m_{11} \\ m_{12} \\ n_1 \end{pmatrix} \quad (4.6)$$

$$\begin{pmatrix} g_0 \\ g_1 \\ \vdots \end{pmatrix} = \begin{pmatrix} B_{c,0} & B_{fl,0} & 1 \\ B_{c,1} & B_{fl,1} & 1 \\ \vdots & \vdots & \vdots \end{pmatrix} \begin{pmatrix} m_{21} \\ m_{22} \\ n_2 \end{pmatrix}, \quad (4.7)$$

where  $\vec{B}_0 = -\mathbf{M}^{-1}(n_1, n_2)^T$ . At first sight, this seems to work perfectly without the problem occurring in a non linear fit, where the start values have to be determined first. However, one faces the problem, that in the parameter fit, only  $g^2$  is determined (only  $g^2$  appears in the transmission formula). Hence, the sign of  $g$  can not be determined.

**Sign Correction:** As we do not know the sign of  $g$ , in a first step the absolute value is taken to get rid of arbitrary signs. For data sets, in which  $B_c$  and  $B_{fl}$  are changed monotonously,  $g$  is expected to change monotonously, which implies, that the sign of  $g$  changes not more than once in such a data set. With this assumption, we can successively try to flip the sign from the  $i$ -th  $g$  to the end of the list (e.g.  $i = 15$  in Fig. 4.3 (a)). If we hit the correct  $i$ , where  $g$  actually changes the sign, then the data should be aligned linear (see Fig. 4.3 (b)). To check, if the data with corrected sign is linear, a linear fit is performed and the residuals of the fits for different  $i$  are compared. Now the list of  $g$  values is overwritten with the corrected list with the smallest residual of the linear fit.

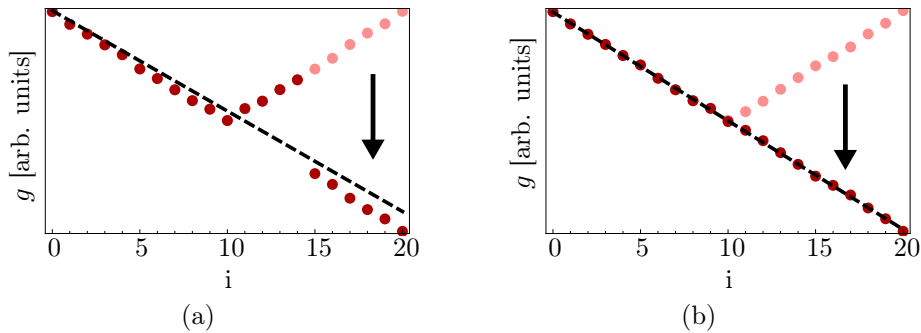


**Fig. 4.3:** Example for the sign correction for a calculated list of  $g$  values. In (a) the linear fit does not match the sign corrected data ( $i = 15$ ), whereas for  $i = 10$  the fit matches and the residual is minimal (the arrow illustrates the sign correction).

This sign correction still lets the choice of an overall sign of the whole list. That gets important as we have two different  $g$ -lists. Therefore, we still have to consider the relative sign of these two lists. This is again done by comparing the residual of the linear least squares fit with the two possible relative signs.

### 4.2.3 Calibration Routine and Results

To generate a data set which can be fitted, the easiest way is to perform a sweep for both  $B_c$  and  $B_{fl}$  around the crossing. Once the B-field matrix is fitted, it is possible to evaluate  $\vec{B}$  for every  $(\Delta, g)$  pair. If necessary, the procedure can be repeated around  $\vec{B}_0$ , to receive more accurate values for  $\vec{B}_0$ . In order to sweep  $\Delta$  and  $g$ , a new LABVIEW program was created, that can set the B-fields and then start a transmission measurement (see section A.1 in Appendix A). This program reads in  $\mathbf{M}$  and  $\vec{B}_0$ , calculates the corresponding  $B_c$  and  $B_{fl}$  for a  $(\Delta, g)$  pair list, sets these voltages and starts the measurements automatically. For fixed  $g$  this works very well, see Fig. 4.4 (a). However, if we try to sweep  $g$  at constant detuning  $\Delta$ , the detuning does not stay constant, it describes a parabola-like function. This is a strong hint, that we need a new model including at least one non linear order.

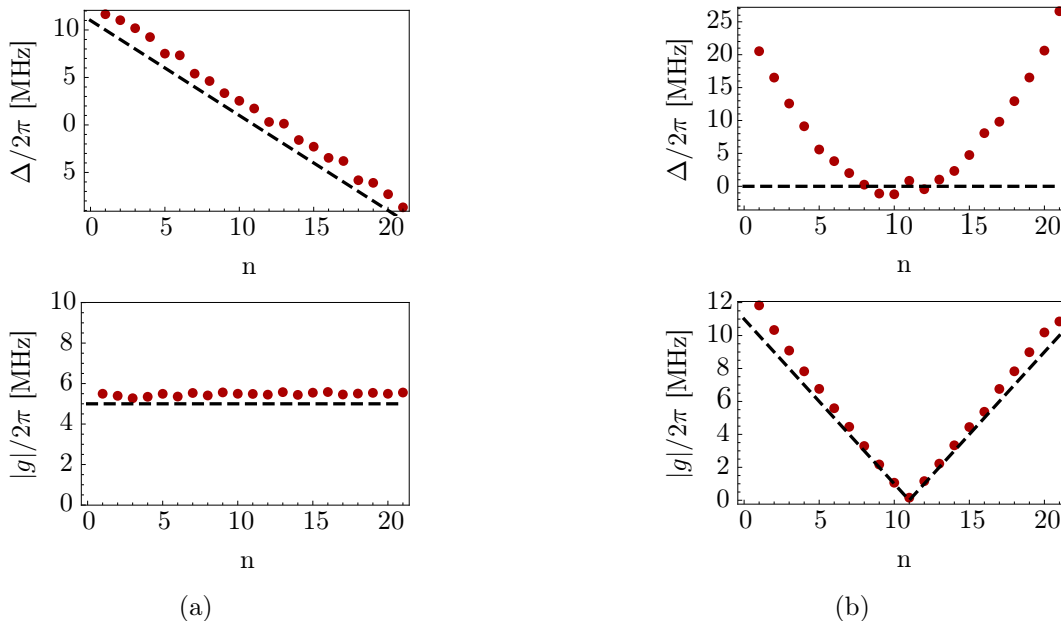


**Fig. 4.4:** (a)  $\Delta$  sweep with  $\Delta \in [-10 \text{ MHz}, 10 \text{ MHz}]$  at fixed  $g = 5 \text{ MHz}$  and (b)  $g$  sweep with  $g \in [-10 \text{ MHz}, 10 \text{ MHz}]$  at fixed  $\Delta = 0 \text{ MHz}$ . The dashed lines are predicted values, and the red dots are the measured values. In (a) the predicted values are well reproduced, whereas in (b)  $g$  takes the desired values and  $\Delta$  fails to be around zero.

## 4.3 Non Linear Model

As the linear model is not accurate enough for sweeps of the coupling strength  $g$  with constant detuning  $\Delta$ , another fit model is needed. At first sight, the deviation of the linear behaviour seems to be a quadratic term (compare Fig. 4.4(b)). Thus, at least one more order is needed in the Taylor expansion to get a better model.

### 4.3.1 Taylor Expansion: New Fit Model

As mentioned above, it offers to expand the function  $(\Delta, g) = f(\vec{B})$  in a Taylor series up to at least second order. The simplest idea would be, to fit the data to this model:

$$\begin{pmatrix} \Delta \\ g \end{pmatrix} = \mathbf{A}(\vec{B} - \vec{B}_0) + \mathbf{B} \begin{pmatrix} (B_c - B_{c,0})^2 \\ (B_{fl} - B_{fl,0})^2 \end{pmatrix} + (B_c - B_{c,0})(B_{fl} - B_{fl,0})\vec{c} \quad (4.8)$$

However, for all these parameters to fit, we only have start values for  $\mathbf{A}$  and  $\vec{B}_0$ . Thus, the MATHEMATICA built-in fit functions fail to find the optimal parameters. Therefore,  $\vec{B}_0$  is not fitted, to reduce the dimension of the parameter space. Instead, an additional parameter  $b_i^0$  is used as offset for the quadratic term in  $\Delta$  and a parameter  $\Delta_{\text{offset}}$  allows an additional, constant offset of the detuning. The model then takes the form

$$\begin{aligned} \Delta &= a_{11}(B_c - B_{c,0}) + a_{12}(B_{fl} - B_{fl,0}) + b_{11}(B_c - B_{c,0} + b_{11}^0)^2 + b_{12}(B_{fl} - B_{fl,0} + b_{12}^0)^2 \\ &\quad + c_1(B_c - B_{c,0})(B_{fl} - B_{fl,0}) + \Delta_{\text{offset}} \end{aligned} \quad (4.9)$$

$$\begin{aligned} |g| &= |a_{21}(B_c - B_{c,0}) + a_{22}(B_{fl} - B_{fl,0}) + b_{21}(B_c - B_{c,0})^2 + b_{22}(B_{fl} - B_{fl,0})^2 \\ &\quad + c_2(B_c - B_{c,0})(B_{fl} - B_{fl,0})|. \end{aligned} \quad (4.10)$$

The crucial idea is, that this fitting routine is designed, such that different data sets can be joined and used as fit data. This makes the fitting routine very flexible, as it allows to add more data, when needed. However, no  $g$  sign correction is possible, since this was only possible for one linear data set (hence, the absolute value is taken). Therefore this models is fitted with the MATHEMATICA built in function `FindMinimum`, with start value  $\mathbf{A}_{\text{start}} = \mathbf{M}$  and all the other start values set to zero. Further, the data where  $g$  is zero is filtered out, since  $\Delta$  can not be fitted when  $g = 0$  (the transmission fit parameters of these measurement sets are not reliable). The main advantage of this new fit routine is, that it can be updated subsequently by adding new data sets. Further, to renew  $\vec{B}_0$ , this can be done by running the old linear fit over two  $B_c/B_{fl}$ -sweep data sets.

### 4.3.2 Calibration Routine and Results

To find the parameters of this model, we first perform a linear fit to calculate  $\vec{B}_0$ . Then, the best way to get reliable values for the model parameters, is to measure a pattern of  $\Delta$  and  $g$  in the range which is later needed (e.g.  $\Delta$  and  $g$  sweeps around  $\Delta = g = 0$ , calculated with the linear model). These data sets are then used to fit the non linear model parameters.

Further, when creating sweep data with this non linear model, one is faced with the discretization of the B-fields (the resolution of the batteries is limited by 1 mV steps). If  $\vec{B}$  is simply rounded to mV, this generates already deviations in  $\Delta$  up to 1 MHz.

To reduce this effect, an algorithm was implemented, that lets  $g$  deviate from the desired value  $g_d$ , and in exchange minimizes the deviation of the calculated detuning  $\Delta$  from the desired value  $\Delta_d$ . E.g. if the allowed deviation of  $g_d$  is 5%, then all  $\vec{B}$ -configurations in the mV-grid with  $|g_d - g(\vec{B})| < 0.05g$  are checked and the one with minimal  $|\Delta_d - \Delta(\vec{B})|$  is

taken. Although, one loses accuracy in  $g$ , the  $\Delta$  values improve massively (see Fig. 4.5(a)).

With this non linear model,  $g$  can be tuned up to 25 MHz, while  $\Delta$  stays now below 3.5 MHz with standard deviation 1.0 MHz (see Fig. 4.5(b)) and for  $g$  tuned around  $\kappa/2\pi \approx 2$  MHz, the detuning is kept close to zero ( $|\Delta| < 0.3$  MHz) (Fig. 4.5 (a)).

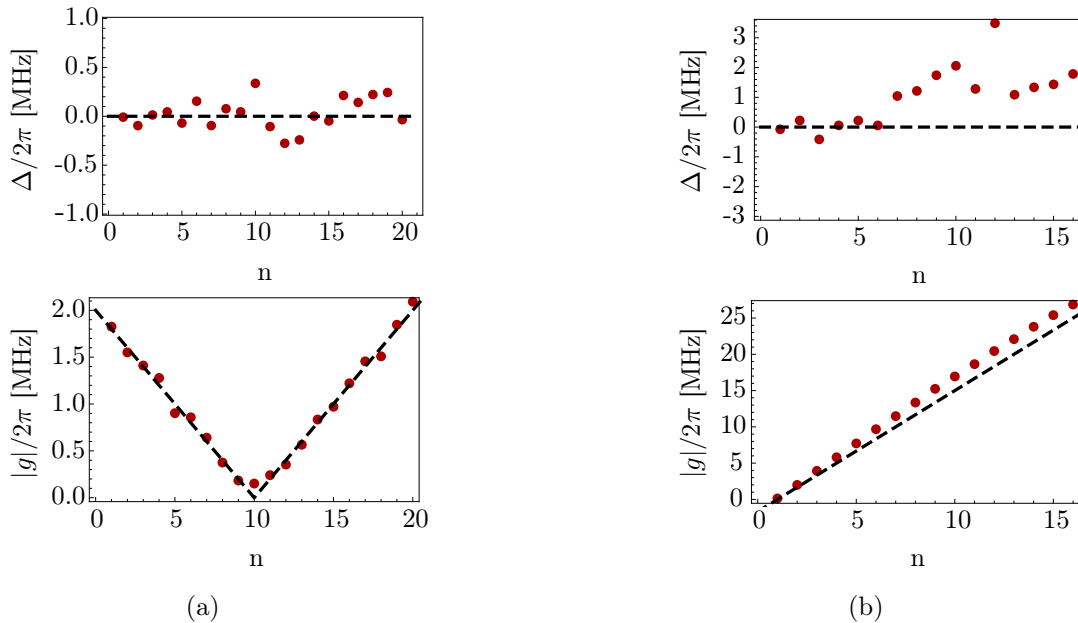


**Fig. 4.5:** (a)  $g$  sweep with  $g/2\pi \in [-2 \text{ MHz}, 2 \text{ MHz}]$  at fixed  $\Delta = 0 \text{ MHz}$  and (b)  $g$  sweep with  $g/2\pi \in [0 \text{ MHz}, 25 \text{ MHz}]$  at fixed  $\Delta = 0 \text{ MHz}$ . The dashed lines are the predicted values, and the red dots are the measured values.

## 4.4 Correlation Function Measurements

In order to characterize a microwave field and especially in the context of the quantum simulation, the correlation functions of the cavity output field need to be measured (compare section 1.2). Here, the correlation functions are characterized and the measurement of the first and second order correlation functions is briefly described.

### 4.4.1 First-Order Correlation Function $G^{(1)}$

The first-order correlation function is defined as the expectation value of the interference of the field at time  $t$  with itself at time  $t + \tau$  [daSilva10]. For the resonator output field the expression is

$$G^{(1)}(t, t + \tau) = \left\langle a_{\text{out}}^\dagger(t) a_{\text{out}}(t + \tau) \right\rangle \quad (4.11)$$

$$G^{(1)}(\tau) = \int_{\mathcal{I}} dt G^{(1)}(t, t + \tau), \quad (4.12)$$

where  $\mathcal{I}$  is a time interval. For our measurements, this time interval does not matter, since the output field is stationary. The first-order correlation function of a coherent field is constant [Bozyigit10].

#### 4.4.2 Second-Order Correlation Function $G^{(2)}$

Similar to the first-order correlation function, the second-order correlation function is defined as [daSilva10]

$$G^{(2)}(t, t + \tau) = \left\langle a_{\text{out}}^\dagger(t) a_{\text{out}}^\dagger(t + \tau) a_{\text{out}}(t + \tau) a_{\text{out}}(t) \right\rangle \quad (4.13)$$

$$G^{(2)}(\tau) = \int_{\mathcal{I}} dt G^{(2)}(t, t + \tau). \quad (4.14)$$

$G^{(2)}$  corresponds to the intensity auto-correlation. Here we measure the correlation function of the resonator output field, when driving the qubit on resonance via qubit charge line with different drive powers and different coupling rates  $g$ , while  $\Delta = 0$ . Since we detect an amplified signal with our measurement setup, we always have to consider the noise added by the amplification chain. If we assume the noise mode to be uncorrelated,  $G^{(1)}(\tau)$  and  $G^{(2)}(\tau)$  can be calculated with reference noise measurements (see e.g. Ref. [Bozyigit10]).

#### 4.4.3 Measurements and Results

The on-resonance driven system can be expressed in a simplified Jaynes-Cummings picture (compare section 2.4.1) by the Hamiltonian

$$H_{\text{sys}} = \hbar g(a^\dagger b + ab^\dagger) + \hbar \Omega(b^\dagger + b), \quad (4.15)$$

where the operators  $a$  and  $b$  and the coupling rate are defined as in section 2.4.1 and  $\Omega$  is the Rabi-rate ( $\Omega^2 \propto$  drive power) [Barrett13]. The correlation function measurements we need for the quantum simulation are therefore done by driving the TCQ on resonance via qubit charge line with different drive powers and coupling rates  $g$  with zero detuning ( $\Delta = 0$ ). The correlation functions are calculated and averaged in real time on the FPGA. This allows us to measure  $G^{(1)}(\tau)$  and  $G^{(2)}(\tau)$ . In the power spectrum  $S(\omega)$ , which is the Fourier transform of  $G^{(1)}(\tau)$ , we can observe so called Mollow triplets as described in Ref. [Lang11]. From the offset of the shoulder peak, the Rabi rate  $\Omega$  can be estimated and related with the drive power (see Fig. 4.6 (a)). Further, although the  $G^{(2)}(\tau)$  measurements show the expected anti-bunching ( $G^{(2)}(0) \leq G^{(2)}(\tau)$ ) for low drive power, they seem to suffer from a feature around  $\tau = 0$  (small dip), which is not expected there, if compared with measurements, e.g. in Ref. [Lang11]. Possible reasons for this feature could be the saturation of the JPD or thermal noise. Since we explicitly need the value  $G^{(2)}(0)$  for the quantum simulation, this problem needs to be further investigated and solved.

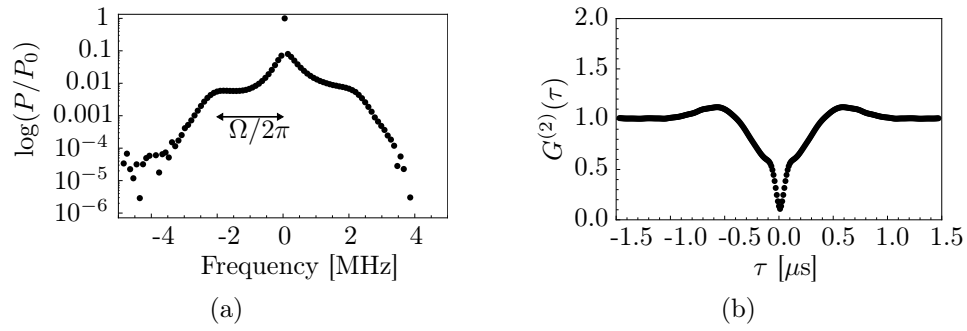


**Fig. 4.6:** (a) Normalized, logarithmic power spectral density of the output field for  $\kappa \approx \Omega \approx 2$  MHz and  $g \approx 0.6$  MHz (drive power  $-38.5$  dBm). (b)  $G^{(2)}(\tau)$  for  $g \approx 0.6$  MHz and drive power  $P = -47.5$  dBm.

# Chapter 5

## Outlook

In summary, we have derived a model to fit a transmission measurement of a qubit coupled to a resonator. Fitting this model to a measurement set, allows to determine all relevant system parameters, such as the detuning  $\Delta$  and the coupling rate  $g$ . This model and fitting routine is applicable not only for the TCQ, but also for other kinds of qubits, coupled to a resonator in very different regimes (from bad cavity limit to strong coupling limit).

Moreover, we have developed a model, which relates detuning  $\Delta$  and coupling  $g$  with the B-field configuration  $\vec{B}$ . This model lets us predict the voltages for a certain  $(\Delta, g)$ -configuration. Even though the calibration for this model works well, it is desirable to correct the qubit frequency before each measurement, since it is very sensitive to disturbances (e.g. vibrations, stray fields), causing slow drifts in the qubit frequency. A correction in  $\Delta$  could be done with the implemented reference measurement in *Sweep-Cleansweep* by calculating the detuning after each measurement and correcting the next B-field configuration with the determined offset. Another hurdle yet to be taken, is the correct determination of the second order correlation function, suffering from a feature around  $\tau = 0$ , as described in section 4.4.3. As mentioned there, possible solutions to this problem are the careful consideration of the saturation of the JPD (e.g. reducing the gain) or the inclusion of thermal noise in the calculations.

If these two improvements are done, we can carry on with the actual quantum simulation. Once the variational energy expression  $E(\lambda)$ , described in section 1.2, can be calculated from the correlation function measurements, this energy has to be minimized. The plan is to measure the correlation functions over a grid of coupling strengths  $g$  and drive powers  $\Omega$  and then minimizing the energy as a function of the scaling factor  $s$  with a standard minimization algorithm. Once the ground state is found, all measurements on the resonator output field can be interpreted as measurements on the one-dimensional Bose gas, i.e. for example the momentum distribution can be measured. Moreover, the only limiting factor to measure higher order correlation function is the detection efficiency. In principle, with high enough detection efficiency all higher order correlation functions could be measured.

In fact, one is not limited to this special type of quantum simulation. This experiment can be understood as a proof of concept for more advanced quantum simulations with more minimization parameters and more complicated systems to be simulated, where classical computers fail and no analytical theories exist.

Furthermore, the TCQ can not only be used for this special purpose of simulating a one-dimensional Bose gas. There are many other applications, where tunable coupling is of interest. For example, by turning the coupling on and off, higher fidelity gates can be reached [Korotkov11]. Moreover, tunable coupling could also be used, when coupling multiple qubits to a single resonator, since it allows to turn the effective qubit-qubit interaction on and off [Gustavsson12]. For all those various applications, the here developed calibration routine can be applied, too.



## Acknowledgement

For providing me the opportunity to perform my Bachelor Thesis at the Quantum Device Lab, I want to thank Professor Andreas Wallraff. I also want to thank my supervisor Dr. Christopher Eichler for teaching me patiently and letting me work independently and Jonas Mlynek for supporting me in Christopher's absence. Furthermore, I want to thank all other team members for helping me out, whenever I needed a helping hand or an advise. Especially Lukas Huthmacher, Marek Pechal, Simon Berger, Anna Stockklauser, Philipp Kurpiers and Yves Salathé I want to thank not only for their support, but also for the pleasant atmosphere.

# Bibliography

- [Barrett13] Barrett, S., Hammerer, K., Harrison, S., Northup, T.E. and Osborn, T.J., Phys. Rev. Lett. **110**, 090501 (2013).
- [Bozyigit10] Bozyigit, D., Master Thesis, ETH Zürich, 2010.
- [daSilva10] da Silva, M.P., Bozyigit, D., Wallraff, A., Blais, A., Phys. Rev. Lett. A **82**, 043804 (2010).
- [Eichler13] Eichler, C., PhD. Thesis, ETH Zürich, 2013.
- [Eichler14] Eichler, C., Salathe, Y., Mlynek, J., Schmidt, S., Wallraff, A., *Quantum limited amplification and entanglement in coupled nonlinear resonators*, arXiv:1404.4643v1 (2014).
- [Feynman82] Feynman, R., *Simulating physics with computers*, Int. J. Theor. Phys. **21**, 467-488 (1982).
- [Gambetta11] Gambetta, J.M., Houck, A.A., Blais, A., Phys. Rev. Lett. **106**, 030502 (2011).
- [Georgescu13] Georgescu, I.M., Ashhab, S., Nori, F., *Quantum Simulation*, arXiv:1308.6263v2 (2013).
- [Gustavsson12] Gustavsson, S., Bylander, J., Yan, F., Forn-Díaz, P., Bolkhovskiy, V., Braje, D., Fitch, G., Harrabi, K., Lennon, D., Miloshi, J., Murphy, P., Slattery, R., Spector, S., Turek, B., Weir, T., Welander, P. B., Yoshihara, F., Cory, D. G., Nakamura, Y., Orlando, T. P., Oliver, W. D., Phys. Rev. Lett. **108**, 170503 (2012).
- [Koch07] Koch, J., Yu, T.M., Gambetta, J., Houck, A.A., Schuster, D.I., Majer, J., Blais, A., Devoret, M.H., Girvin, S.M., Schoelkopf, R.J., Phys. Rev. Lett. A **76**, 042319 (2007).
- [Korotkov11] Korotkov, A.N., Phys. Rev. B **84**, 014510 (2011).
- [Lang11] Lang, C., Bozyigit, D., Eichler, D., Steffen, L., Find, J.M., Abdumalikov, A.A., Jr., Baur, M., Filipp, S., da Silva, M.P., Blais, A., Wallraff, A., Phys. Rev. Lett. **106**, 243601 (2011).
- [Lieb63] Lieb, E.H., Liniger, W., Phys. Rev. **130**, 1605-1616 (1964).

[Srinivasan11] Srinivasan, S.J., *et al.*, Phys. Rev. Lett. **106**, 083601 (2011).

[Walls08] Walls, D.F., Milburn, G.J., *Quantum Optics*, (Springer 2008) 2nd Ed.

[Winterer13] Winterer, F., Semester Thesis, ETH Zürich, 2013.

# Appendix A

## Measurement Software

To run standard measurements, a LabVIEW program (**Cleansweep**) was used. This software allows to perform two dimensional, linear sweeps (e.g. B-field vs. frequency). For sweeps in  $\Delta$  or  $g$  with the above developed linear and non linear model, both coil and flux-line have to be swept (not necessarily linear). Therefore, a new LabVIEW program **SweepCleansweep** was written, that can independently set the output power and  $\vec{B}$  (i.e. coil and flux-line separately) and then run **Cleansweep** with an entered configuration file from a previous **Cleansweep** measurement.

### A.1 SweepCleansweep

As mentioned above, the main application of this program **SweepCleansweep** is reading in a configuration file, changing the B-fields and the output power of the microwave generator and then running **Cleansweep** with these modified configurations. In file handling (1) (compare Fig. A.1), the path of the config-file has to be entered. Further, the path where the measurement data is stored and the first file number have to be specified. In general settings (2) the slots of the SRS batteries and the microwave generator (for the output power) are entered. An important part is the sweep generation. This is done in (3) (see Fig. A.1), where one can choose between reading in a B-field list or generating it with the calculated B-field matrix and  $\vec{B}_0$ . In (4) an optional reference measurement with separate config-file can be enabled (e.g. when correlation functions are measured, then after each measurement a resonator spectroscopy can be measured to monitor  $\Delta$  and  $g$ ).

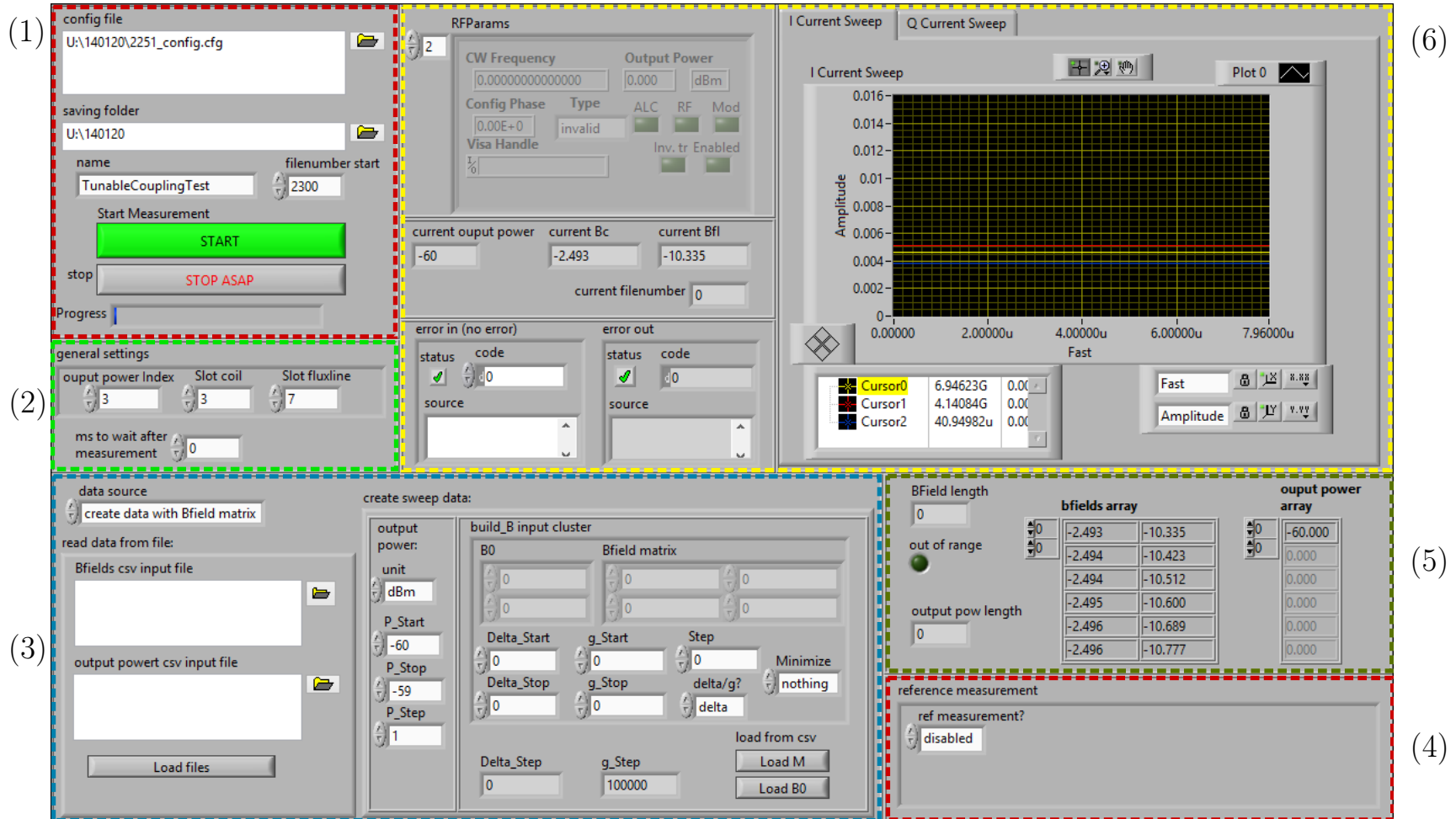


Fig. A.1: LABVIEW program with file handling (1), general settings (2), sweep (3), reference measurement (4), sweep information (5) and general information (6).